

Diff2DGS: Reliable Reconstruction of Occluded Surgical Scenes via 2D Gaussian Splatting

Tianyi Song¹, Danail Stoyanov², Evangelos Mazomenos³ and Francisco Vasconcelos⁴

Abstract—Real-time reconstruction of deformable surgical scenes is vital for advancing robotic surgery, improving surgeon guidance, and enabling automation. Recent methods achieve dense reconstructions from da Vinci robotic surgery videos, with Gaussian Splatting (GS) offering real-time performance via graphics acceleration. However, reconstruction quality in occluded regions remains limited, and depth accuracy has not been fully assessed, as benchmarks like EndoNeRF and StereoMIS lack 3D ground truth. We propose Diff2DGS, a novel two-stage framework for reliable 3D reconstruction of occluded surgical scenes. In the first stage, a diffusion-based video module with temporal priors inpaints tissue occluded by instruments with high spatial-temporal consistency. In the second stage, we adapt 2D Gaussian Splatting (2DGS) with a Learnable Deformation Model (LDM) to capture dynamic tissue deformation and anatomical geometry. We also extend evaluation beyond prior image-quality metrics by performing quantitative depth accuracy analysis on the SCARED dataset. Diff2DGS outperforms state-of-the-art approaches in both appearance and geometry, reaching 38.02 dB PSNR on EndoNeRF and 34.40 dB on StereoMIS. Furthermore, our experiments demonstrate that optimizing for image quality alone does not necessarily translate into optimal 3D reconstruction accuracy. To address this, we further optimize the depth quality of the reconstructed 3D results, ensuring more faithful geometry in addition to high-fidelity appearance. The code is available in <https://anonymous.4open.science/r/Diff2DGS>.

I. INTRODUCTION

Intraoperative 3D reconstruction of surgical scenes is essential for advancing robot-assisted surgery. High-precision, dynamic 3D reconstruction enables surgical robotic systems to enhance instrument control accuracy, thereby supporting key clinical applications such as real-time surgical navigation [1], [2], autonomous robotic assistance [6], and surgeon training simulation [7], [8].

Early approaches to surgical scene reconstruction relied on techniques such as depth estimation [33], [35], simultaneous localization and mapping (SLAM) [19], and point cloud fusion [36]. With the emergence of Neural Radiance Fields (NeRF) [10], subsequent research has shifted toward representing surgical scenes as dense neural light fields [11], [12]. For example, Lerplane [9] models the dynamic characteristics of surgical scenes by representing them as 4D spatiotemporal volumes, significantly improving reconstruction fidelity. Despite these advancements, NeRF-based methods tend to be computationally heavy, making them impractical for real-time intraoperative reconstruction.

With advancements in computer graphics, 3D Gaussian Splatting (3DGS) [15] has emerged as a breakthrough that significantly improves the efficiency of dense 3D scene

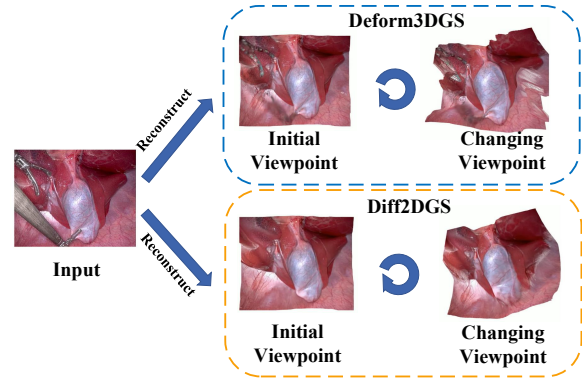


Fig. 1. Traditional endoscopic scene reconstruction methods often focus solely on image quality from the camera viewpoint, neglecting the depth accuracy of the reconstruction results. Consequently, when the camera viewpoint changes, reconstruction accuracy degrades significantly. We present Diff2DGS, a framework that effectively balances depth information and image quality, achieving high-quality 3D reconstruction while more effectively eliminating artifacts in occluded regions and providing more accurate depth estimation.

reconstruction. Initially designed for static 3D reconstruction, 3DGS has been extended in subsequent studies to handle dynamic 3D scenes [16], [17]. For instance, 4DGS [14] introduced a temporal deformation framework that correlates scene dynamics with time, leveraging a feature plane decomposition approach akin to HexPlane [18] to model dynamic environments. However, 4DGS underutilizes geometric priors, resulting in excessively sparse point initialization and prolonged reconstruction times.

To address the pervasive challenge of tissue deformation in intraoperative scenarios, recent methods such as EndoGaussian [21], [13] and Deform3DGS [20] leverage deformation fields combined with efficient voxel encoding and lightweight deformation decoders to achieve real-time surgical scene reconstruction with dynamic tissue modeling. For instance, Endo-4DGS [13] incorporates monocular depth priors generated by Depth Anything [22] and introduces a confidence-guided learning strategy to mitigate uncertainties in monocular depth estimation. Similarly, Deform3DGS [20] models tissue deformation through efficient linear combination regression with learnable basis functions, enhancing representational capacity and computational efficiency. However, we verify that these methods still struggle to reconstruct details in regions occluded by surgical instruments. Furthermore, evaluation of these methods is still limited to datasets that do not have 3D reconstruction groundtruth (EndoNeRF, StereoMIS) and rely on re-projected image quality metrics

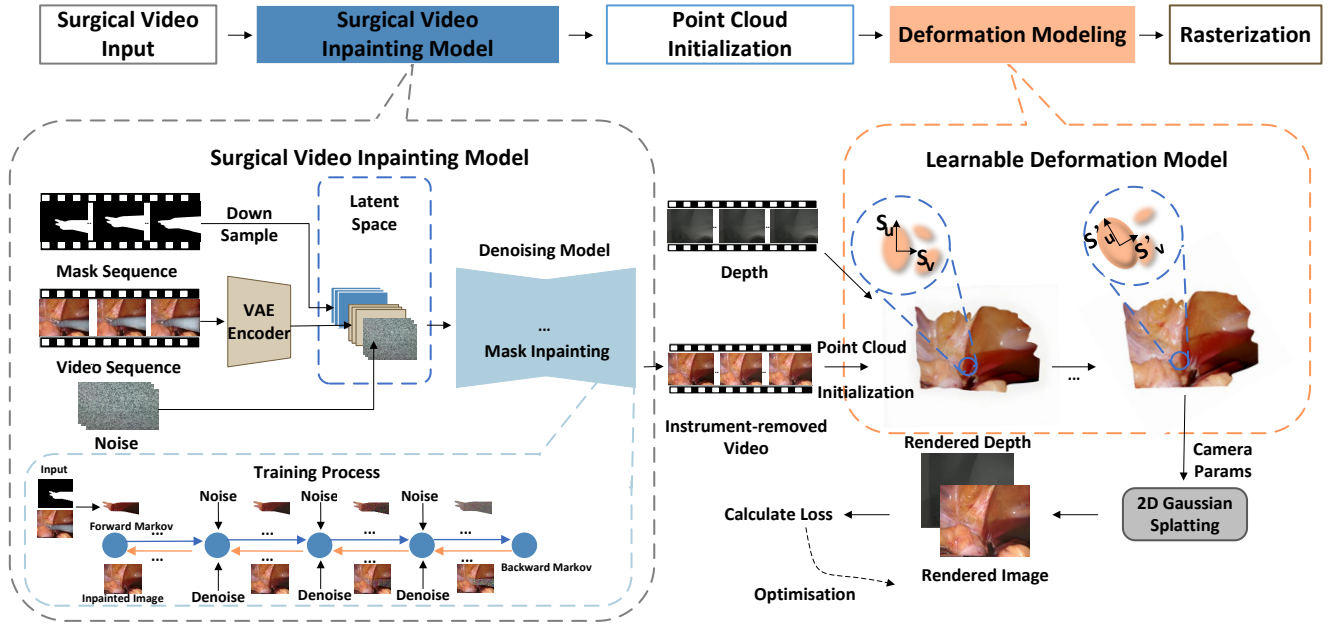


Fig. 2. Our reliable surgical scene reconstruction framework, Diff2DGS, consists of Surgical Instrument Inpainting, Point Cloud Initialization, Deformation Modeling, and 2D Gaussian Splatting.

such as Structured Similarity (SSIM) and Peak Signal-to-Noise ratio (PSNR). As we show in our work, good results in these metrics do not necessarily mean accurate reconstruction. To the best of our knowledge, there are no public datasets of surgical video that include both severe tissue deformation and accurate 3D reconstruction groundtruth. Nonetheless, there are a few established benchmarks for 3D reconstruction with surgical data such as SCARED and Serv-CT. In particular, Serv-CT provides volumetric CT data of surgical scenes with corresponding annotations, enabling evaluation of reconstruction methods in scenarios involving intra-operative imaging. SCARED, on the other hand, includes stereo video from a surgical robot paired with 3D anatomy groundtruth acquired with a structured-light camera and therefore has high potential as an evaluation tool for the recent literature on Gaussian Splatting 3D reconstruction.

Our method relies on inpainting anatomy regions occluded by surgical instruments. Recent state-of-the-art methods in this domain exploit diffusion models [23], [24] for high-quality video restoration. However, these methods often suffer from hallucination artifacts inherent to diffusion models. To mitigate this, methods such as FloED [25], FFF-VDI [26], and DiffuEraser[37] employ different strategies to incorporate temporal consistency and reduce hallucination.

This paper proposes Diff2DGS, a two-stage framework for deformable intraoperative 3D reconstruction. First, we enhance diffusion-based mask inpainting by integrating temporal video priors to restore tissues occluded by surgical instruments. Next, we apply the 2D Gaussian Splatting (2DGS) [27] method to surgical scenes using a learnable deformable model (LDM) that explicitly accounts for dynamic tissue deformation and anatomical geometry. The depth information of the reconstruction results is further

optimized using adaptive depth loss weights to achieve high-fidelity reconstruction. We evaluate Diff2DGS on three publicly available datasets utilising the da Vinci robotic system: EndoNeRF [11], StereoMIS [28], and SCARED. Overall, our main contributions are as follows:

- We present Diff2DGS, a novel two-stage framework that explicitly inpaints surgical instruments on 2D images prior to 3D reconstruction, thereby effectively reducing artifacts in occluded regions.
- We extend the 2D Gaussian representation to deformable tissue reconstruction and introduce a Learnable Deformation Model (LDM). Compared to parameter-heavy approaches such as Deform3DGS [20] and Endo-4DGS [13], this design improves efficiency while maintaining reconstruction fidelity.
- We propose an adaptive depth loss that dynamically adjusts depth weighting during training, leading to improved geometric accuracy.
- We comprehensively validate the superior performance of Diff2DGS through quantitative and qualitative evaluations, achieving 38.02 dB PSNR on the EndoNeRF dataset and 33.90 dB PSNR on the StereoMIS dataset.

II. METHOD

The overall framework of Diff2DGS is depicted in Fig. 2. First, we use a diffusion model to remove surgical instruments and inpaint them with the tissue underneath. This process utilises surgical instrument segmentation across frames and generates high quality tissue images with spatiotemporal consistency using stable diffusion and temporal attention (Section 2.3). Inpainted images are then combined with stereo depth information to initialize a Gaussian point cloud,

and tissue deformation is simulated by a Learnable Deformation Model (Section 2.2). Subsequently, a 2D Gaussian splatting model is applied to generate a color image and depth map from the perspective of the given camera, which is further refined through optimisation.

A. Preliminaries of Gaussian Splatting

3D Gaussian Splatting (3DGS) was originally proposed to model static scenes[15] as a set of 3D Gaussian intensity distributions that can be projected to arbitrary 2D viewpoints. Each Gaussian is characterized by its 3D position μ and 3×3 covariance matrix Σ encoding its scale (S) and orientation (R) in world coordinates. For any 3D point $x = (x, y)$ in world coordinates, the impact of a 3D Gaussian on x is defined by the Gaussian distribution:

$$G^{3D}(x) = \exp\left(-\frac{1}{2}(x - \mu)^T \Sigma^{-1}(x - \mu)\right) \quad (1)$$

$$\Sigma^{3D} = RSS^T R^T \quad (2)$$

Giving the world-to-camera transformation matrix \mathbf{W} , in the rendering process, the covariance matrix can be projected into image space as:

$$\Sigma^{r3D} = \mathbf{J}\mathbf{W}\Sigma^{3D}\mathbf{W}^T\mathbf{J}^T \quad (3)$$

where \mathbf{J} is the Jacobian of the affine approximation of the projective transformation. However, 3D Gaussians are often suboptimal as a representation of surface textures and edges. To mitigate this, a 2D Gaussian[27] representation proposes instead to model a scene in terms of planar Gaussians embedded in 3D space. Each 2D Gaussian is represented by a central point \mathbf{p}_c , its 2D plane defined as two orthogonal tangent vectors t_u and t_v , and the scale along the tangent directions $S = (s_u, s_v)$. Any 3D point P in world coordinates can be parametrised in terms of u, v 2D coordinates in the tangent plane:

$$P(u, v) = \mathbf{p}_c + s_u t_u u + s_v t_v v = \mathbf{H}(u, v, 1, 1)^T \quad (4)$$

$$\mathbf{H} = \begin{bmatrix} s_u t_u & s_v t_v & 0 & \mathbf{p}_c \\ 0 & 0 & 0 & 1 \end{bmatrix} = \begin{bmatrix} \mathbf{R}\mathbf{S} & \mathbf{p}_c \\ 0 & 1 \end{bmatrix} \quad (5)$$

where \mathbf{H} is a homogeneous transformation matrix representing the geometry of the 2D Gaussian. R is a 3×3 rotation matrix $[t_u, t_v, t_u \times t_v]$ and S is a 3×3 diagonal matrix whose last entry is zero.

The 2D Gaussian G^{2D} can be represented as a 2×2 covariance matrix Σ'^{2D} in uv space, which is skipping the third row and column of Σ'^{3D} in (3). For the point $\mathbf{u} = (u, v)$ in uv space, its 2D Gaussian value can be evaluated by standard Gaussian:

$$G^{2D}(\mathbf{u}) = \exp\left(-\frac{1}{2}\mathbf{u}^T (\Sigma'^{2D})^{-1} \mathbf{u}\right) = \exp\left(-\frac{u^2 + v^2}{2}\right) \quad (6)$$

The rasterization process in 2DGS is similar to that in 3DGS, both employing volumetric alpha blending to integrate alpha-weighted appearance from front to back:

$$C(\mathbf{x}) = \sum_{i=1}^N G_i^{2D}(\mathbf{x}) \alpha_i c_i \prod_{j=1}^{i-1} (1 - G_j^{2D}(\mathbf{x}) \alpha_j) \quad (7)$$

where α_i represents the opacity and c_i denotes the color of each Gaussian primitive.

B. Learnable Deformation Model for 2D Gaussian Splatting(LDM)

The original 2D Gaussian Splatting (2DGS) is limited to reconstructing static scenes. Therefore, we propose a learnable deformation model (LDM) that follows a similar strategy to Deform3DGS[20], but utilises a 2D Gaussian representation for better reconstruction of tissue surfaces. Specifically, we employ Gaussian functions with learnable centers θ and variances σ for estimating tissue deformation.

$$\tilde{G}'(t; \theta, \sigma) = \exp\left(-\frac{1}{2\sigma^2}(t - \theta)^2\right) \quad (8)$$

Here, t denotes time. For each Gaussian g_i in the point cloud, the position p_C and the rotation R are directly related to tissue deformation. The scale S varies as tissues experience elastic deformations during instrument intervention. Therefore, we have established a set of learned parameters $\Theta^S, \Theta^R, \Theta^{p_c}$ to describe deformation through scale, rotation, and position. As described in Eq. (5), we map the matrices R and S to the 2D parameters $s_u, t_u, s_v,$ and t_v . Consequently, Θ^S and Θ^R can be further decomposed into $\Theta^{s_u}, \Theta^{s_v}, \Theta^{t_u},$ and Θ^{t_v} . Taking the scale S change in u direction as an example, the Θ^{S_u} can be define as the deformation of S in u direction, the new scale in u direction S'_u is:

$$S'_u = S_u + \Theta^{S_u} = S_u + \sum_{j=1}^B \omega_j^{S_u} \tilde{G}'(t; \theta_j^{S_u}, \sigma_j^{S_u}) \quad (9)$$

By integrating the deformation variables, the LDM ensures smooth transitions and continuity in deformation across adjacent time points, maintaining a coherent and consistent temporal progression.

C. Diffusion-based Inpainting of Surgical Instruments

Tissue 3D reconstruction is made challenging by the presence of surgical instruments that partially occlude the view. Previous works have addressed this by utilising surgical instrument segmentation to mask out instrument regions during 3D reconstruction optimisation with NeRF or Gaussian Splatting representations. We instead propose to use a diffusion model[30] as a pre-processing step to remove surgical instrument occlusions and inpaint them with the tissue appearance underneath. We then perform 3D reconstruction without masking out any region.

The video inpainting model categorizes pixels into two types: known pixels (non-occluded tissue) that are propagated using temporal information from preceding frames, and unknown pixels (occluded tissue) that are generated

TABLE I
COMPARISON BETWEEN DIFF2DGS AND EXISTING METHODS ON ENDOnerf.

Models	EndoNeRF-Cutting				EndoNeRF-Pulling				FPS
	PSNR \uparrow	SSIM (%) \uparrow	LPIPS \downarrow	RMSE \downarrow	PSNR \uparrow	SSIM (%) \uparrow	LPIPS \downarrow	RMSE \downarrow	
EndoNeRF [11]	35.84	94.25	0.085	4.299	35.43	93.89	0.077	4.746	0.03
LerPlane [9]	35.21	92.96	0.095	5.782	34.87	91.94	0.118	6.245	0.93
EndoGaussian [21]	37.19	95.29	0.052	4.032	35.98	94.23	0.047	5.341	83.13
Deform3dgs [20]	37.33	95.89	0.075	4.234	<u>37.70</u>	<u>95.57</u>	0.069	5.727	<u>228.58</u>
SurgicalGS [31]	37.93	96.19	<u>0.045</u>	1.779	<u>37.13</u>	<u>95.43</u>	<u>0.062</u>	2.193	154.39
Diff2DGS (Ours)	38.23	96.76	0.033	<u>2.443</u>	37.81	96.12	0.042	<u>2.574</u>	232.29

TABLE II
COMPARISON BETWEEN DIFF2DGS AND EXISTING METHODS ON STEREOmIS.

Models	StereoMIS-P2.7				StereoMIS-P3				FPS
	PSNR \uparrow	SSIM (%) \uparrow	LPIPS \downarrow	RMSE \downarrow	PSNR \uparrow	SSIM (%) \uparrow	LPIPS \downarrow	RMSE \downarrow	
EndoNeRF [11]	28.87	80.23	0.259	4.354	28.33	80.09	0.287	4.165	0.06
LerPlane [9]	29.53	78.36	0.205	8.356	29.41	78.14	0.213	7.983	0.05
EndoGaussian [21]	31.11	87.29	<u>0.127</u>	9.793	31.03	87.13	0.136	8.932	0.93
Deform3dgs [20]	<u>31.83</u>	87.75	0.129	10.036	30.91	87.73	<u>0.131</u>	8.482	214.38
SurgicalGS [31]	31.63	<u>88.26</u>	0.152	2.747	<u>31.49</u>	<u>87.75</u>	0.925	2.536	154.82
Diff2DGS (Ours)	34.72	91.17	0.113	<u>3.874</u>	34.08	90.27	0.131	<u>3.717</u>	<u>212.32</u>

by the diffusion model while preserving structural integrity. To further enhance consistency in long video sequences, a temporal attention mechanism is utilised to extend the model’s temporal receptive field. The temporal attention mechanism TA_t can be defined as:

$$\begin{aligned}
 TA_t &= \text{TemporalAttention}(Q_t, K_t, V_t) \\
 &= \text{Softmax}\left(\frac{\mathbf{Q}_t \mathbf{K}_t^\top}{\sqrt{d_k}} + \mathbf{M}_t\right) \mathbf{V}_t
 \end{aligned} \quad (10)$$

where $\mathbf{Q}_t, \mathbf{K}_t, \mathbf{V}_t$ are linearly projected features from latent space, d_k denotes the head dimension, and \mathbf{M}_t is a causal mask[34] with $(\mathbf{M}_t)_{ij} = 0$ if $i \geq j$ and $(\mathbf{M}_t)_{ij} = -\infty$ otherwise.

We optimize the diffusion-based inpainting module using a mask-weighted L2 loss in the latent space. Given a clean latent \mathbf{z}_0 and timestep t , we construct a noisy latent \mathbf{z}_t by the forward diffusion process, i.e., $\mathbf{z}_t = \sqrt{\bar{\alpha}_t} \mathbf{z}_0 + \sqrt{1 - \bar{\alpha}_t} \boldsymbol{\epsilon}$ with $\boldsymbol{\epsilon} \sim \mathcal{N}(\mathbf{0}, \mathbf{I})$. The denoising network $\hat{\boldsymbol{\epsilon}}_\theta$ predicts the injected noise conditioned on the masked inputs and temporal priors, denoted by \mathbf{c} . Let \mathbf{m} be a binary inpainting mask downsampled to the latent resolution (with $\mathbf{m} = 1$ indicating the occluded/inpainted region). The training loss is:

$$\mathcal{L}_{\text{inpaint}} = \mathbb{E}_{\mathbf{z}_0, t, \boldsymbol{\epsilon}} \left[\left\| \mathbf{m} \odot \left(\boldsymbol{\epsilon} - \hat{\boldsymbol{\epsilon}}_\theta(\mathbf{z}_t, t, \mathbf{c}) \right) \right\|_2^2 \right], \quad (11)$$

where \odot denotes the Hadamard product. This objective emphasizes accurate restoration inside the masked region while maintaining global structural coherence.

For inference, we adopt the DDIM [30] sampling strategy. We first estimate the clean latent $\hat{\mathbf{z}}_0$ at each step:

$$\hat{\mathbf{z}}_0 = (\mathbf{z}_t - \sqrt{1 - \bar{\alpha}_t} \hat{\boldsymbol{\epsilon}}_\theta(\mathbf{z}_t, t, \mathbf{c})) / \sqrt{\bar{\alpha}_t}. \quad (12)$$

Then, the latent at the previous timestep \mathbf{z}_{t-1} is computed as:

$$\mathbf{z}_{t-1} = \sqrt{\bar{\alpha}_{t-1}} \hat{\mathbf{z}}_0 + \sqrt{1 - \bar{\alpha}_{t-1}} \hat{\boldsymbol{\epsilon}}_\theta(\mathbf{z}_t, t, \mathbf{c}). \quad (13)$$

D. Adaptive Depth Loss Weight

As shown in Fig 1, Gaussian Splatting often produce reconstructions with sharp depth changes that do not correspond to an accurate representation of the tissue shape.

To enhance the model’s attention to depth accuracy, we adopt an adaptive depth loss weighting strategy that dynamically adjusts the weight of the depth loss throughout the training process.

Specifically, in 3D reconstruction tasks, we aim to simultaneously minimize the RGB reconstruction error L_{rgb} and the depth reconstruction error L_{depth} .

$$\mathcal{L} = L_{\text{rgb}} + \lambda_{\text{depth}} L_{\text{depth}} \quad (14)$$

Here, λ_{depth} is a fixed parameter. However, using fixed weights makes it difficult to balance the dynamic range and convergence speed of both losses. In the early stages of training, the RGB loss often dominates, whereas in the later stages, the depth loss may become more significant. To address this, we propose an adaptive depth loss weight that can automatically adjust λ_{depth} during the training process.

To prevent the depth term from becoming overly dominant in the later stages of training, we first define a base weight that decays linearly with the number of iterations.

$$w_{\text{base}}(t) = w_{\text{init}} \left(1 - \alpha \frac{t}{T} \right), \quad 0 \leq t \leq T, \quad (15)$$

Here, w_{init} is the initial weight, T is the total number of iterations, and $\alpha \in [0, 1]$ controls the attenuation amplitude (with a default value of $\alpha = 0.5$).

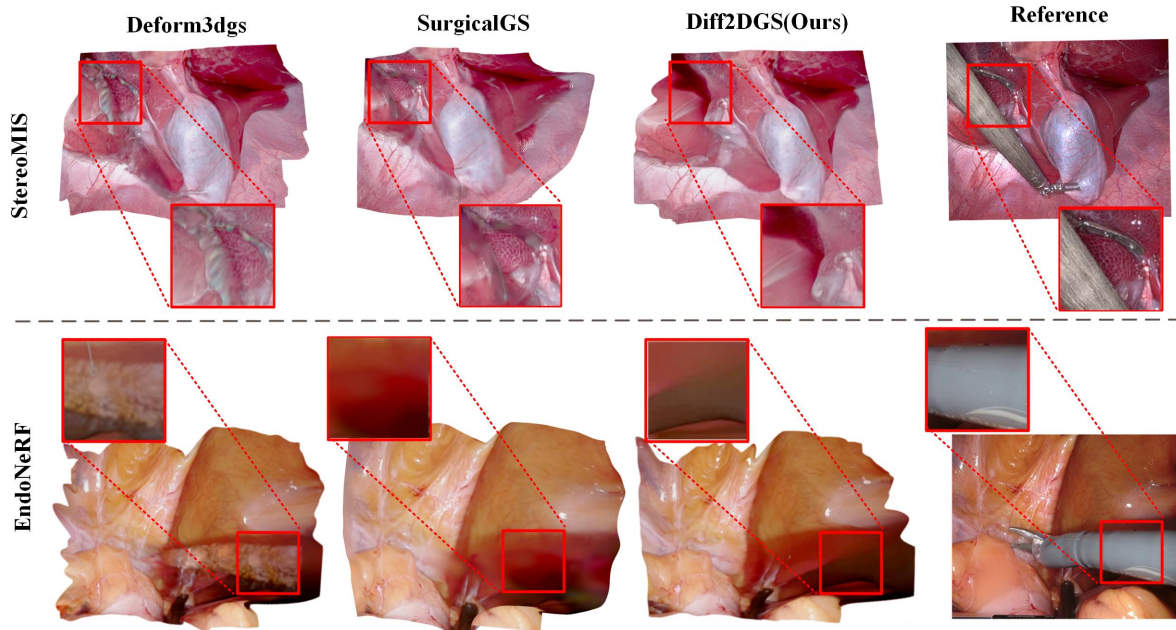


Fig. 3. Visualization of the 3D reconstruction results.

We dynamically adjust the depth loss weight based on the loss ratio, which can be formulated as:

$$r(t) = \frac{L_{\text{rgb}}(t)}{L_{\text{depth}}(t) + \varepsilon}, \quad \varepsilon = 10^{-8} \quad (16)$$

When $r(t) > 1$, it indicates that the RGB loss is greater than the depth loss, and the depth weight should be increased; otherwise, it should be decreased. To achieve smooth adjustment, we introduce the hyperbolic tangent function:

$$g(r(t)) = 1 + \beta \tanh(r(t) - 1), \quad \beta \in (0, 1]. \quad (17)$$

The final weight can be expressed as:

$$\lambda_{\text{depth}}(t) = \text{clip}(w_{\text{base}}(t)g(r(t)), w_{\text{min}}, w_{\text{max}}) \quad (18)$$

Here, $\text{clip}(x, a, b) = \min(\max(x, a), b)$. The weights are constrained to the interval $[w_{\text{min}}, w_{\text{max}}]$, where $w_{\text{min}} = w_{\text{final}}$ and $w_{\text{max}} = 2w_{\text{init}}$ in our research.

III. EXPERIMENTS

A. Experiment Setting

Datasets and Evaluation: We evaluate the proposed method and compare it with existing works on EndoNeRF [11], StereoMIS [28] and SCARED [32] datasets.

The EndoNeRF is a collection of stereo endoscopic videos, including 6 clips extracted from Da Vinci robotic prostatectomy data. The StereoMIS is a stereo endoscopic video dataset captured from in-vivo porcine subjects, containing diverse anatomical structures and challenging scenes with large tissue deformations. The masks of EndoNeRF and StereoMIS are both provided in the datasets. For both

these datasets we evaluate methods using image similarity metrics (PSNR, SSIM, LPIPS) in line with previous literature using these datasets [20], [21]. However, our results suggest that image similarity is not sufficient to fully evaluate 3D reconstruction accuracy and should be complemented with geometry-based metrics. Given that neither of these datasets has 3D shape groundtruth, we provide depth difference (RMSE) between methods' estimates and stereo reconstructions (RAFT [38]). Additionally, we evaluate our method on the SCARED dataset, which has depth groundtruth obtained with a structured light sensor. It contains images of five porcine cadaver abdominal anatomies acquired with a DaVinci endoscope. Unlike EndoGaussian [21], which evaluates only the regions overlapping with a reference view by masking newly visible areas introduced by camera motion, we report metrics on the entire reconstructed scene. For a fair comparison, all methods including EndoGaussian, are re-evaluated under this unified protocol.

Experiment Details: The inpainting module is built upon Stable Diffusion v1.5 and comprises approximately 2.47B parameters in total. We use Phased Consistency Model (PCM[3]) to accelerate the diffusion inference stage, which only requires two denoising steps per frame to perform mask inpainting. The model is fine-tuned on surgical sequences of SCARED dataset where supervision is provided by a mask-weighted L_2 loss with the learning rate of $1e-5$. For the gaussian splatting module, we normalize the video duration for each scene into the range $[0, 1]$. The training runs for 6000 iterations with an initial learning rate of 3.2×10^{-3} . To stabilize training, we freeze the number of Gaussian points

during the initial 600 iterations. All experiments are implemented using the PyTorch framework[29] and conducted on a single NVIDIA Tesla V100 GPU.

B. Comparison with State-of-the-art Methods

To ensure a fair and consistent comparison, we evaluate the proposed Diff2DGS framework alongside existing state-of-the-art methods under the same experimental environment and hardware configurations. As shown in Table I and Table II, our framework outperforms Deform3DGS [20] on both EndoNeRF and StereoMIS datasets, demonstrating the value of a 2D Gaussian parametrisation. The more recent method SurgicalGS[31] produces reconstructions closer to RAFT stereo reconstructions (RMSE). However, we note that this method has additional depth priors based on RAFT[38] estimates and that it has a slower rendering speed. As a Gaussian splatting method, our framework’s rendering speed is hundreds of times faster than NeRF-based methods such as EndoNeRF and LerPlane. When compared to other Gaussian splatting methods, Diff2DGS achieves rendering speeds comparable to Deform3DGS while improving reconstruction results in occluded regions. As a result, our framework provides a favourable balance between reconstruction quality and rendering speed.

Fig. 3 shows rendered surgical scenes for visual evaluation comparing our method with Deform3DGS and SurgicalGS. We observe that both Deform3DGS and SurgicalGS exhibit significant artifacts in occluded regions. In contrast, our method achieves superior image similarity metrics primarily due to more accurate reconstruction of instrument-occluded areas, demonstrating the effectiveness of diffusion-based inpainting.

To validate the improvement in masked regions, we synthetically overlay surgical instrument masks on the SCARED dataset, using the original unmasked images as ground truth. As shown in the updated Table III and the Figure 5, Diff2DGS demonstrates significant advantages in occluded regions, achieving PSNR of 30.53 dB and RMSE of 8.21 mm—substantially outperforming Deform3DGS, EndoGaussian, and SurgicalGS, and further improving upon the inpainting baseline.

To assess temporal stability, we define the Temporal Consistency (TC) as the average root mean squared error (RMSE) between all consecutive frame pairs in a sequence. While the TC of the ground truth (TC_{GT}) reflects the natural dynamics of the scene, we evaluate the fidelity of our results using the Temporal Consistency Score (TCS):

$$TCS = |TC_{result} - TC_{GT}| \quad (19)$$

A lower TCS indicates that the generated video better preserves the original temporal characteristics. As shown in the updated Table III, our inpainting module achieves the best temporal consistency, while our final method attains suboptimal performance—yet remains superior to all other compared methods.

Fig. 4 shows qualitative reconstruction results comparing our Diff2DGS method with Deform3DGS on the SCARED

dataset. It can be observed that once the camera viewpoint changes, the depth information disadvantage of Deform3dgs becomes more pronounced, and our model effectively addresses this issue.

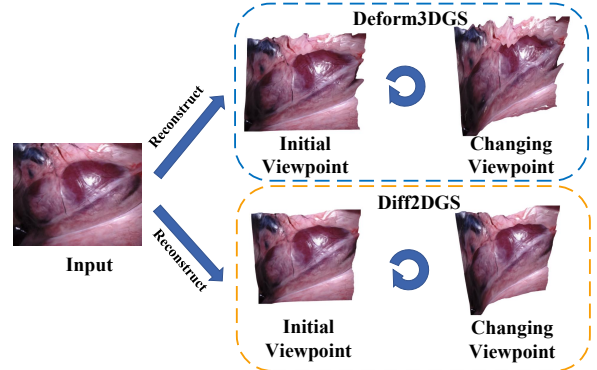


Fig. 4. Depth Quality Visualization on SCARED Dataset

C. Ablation experiment

To verify the effectiveness of each module in Diff2DGS, we designed several variant models and conducted experiments on the StereoMIS dataset. The results are shown in Table IV.

To validate the effectiveness of the “Surgical Video Inpainting” module, we created a variant “Diffusion + Deform3DGS” by removing the mask processing from Deform3DGS and using the inpainting module as prior information. We noticed that this method significantly improved the model’s performance on the StereoMIS dataset, further demonstrating the effectiveness and flexibility of the “Surgical Video Inpainting” module. In the “w/o deformation” variant, we remove the Learnable Deformation Model (LDM) to assess its contribution. Results show significant performance degradation, confirming the importance of the LDM. Additionally, the visualization results revealed a noticeable reduction in the quality of the rendered deformed tissue. The same decline also occurs in ‘w/o inpainting’ when we remove the inpainting module. Therefore, through ablation experiments, we validated the effectiveness of each module in the framework.

Fig. 6 visualizes the ablation study on the EndoNeRF dataset. Compared to the full model (Col. 2), removing the Learnable Deformation Model (LDM) (Col. 3) leads to significant detail loss and blurring, while omitting the inpainting module (Col. 4) results in severe artifacts, particularly in regions occluded by surgical instruments. Furthermore, comparing our 2DGS-based approach with the inpainting-enhanced Deform3DGS (Col. 5) demonstrates that while inpainting effectively mitigates occlusion artifacts for both, our method yields more realistic textures and consistent geometric details in the reconstructed areas.

D. Error analysis of RAFT

Since neither EndoNeRF nor StereoMIS provides ground truth depth for occluded regions, and StereoMIS depth maps are derived from RAFT [38], we follow prior work and use

TABLE III
QUANTITATIVE COMPARISON OF DIFFERENT METHODS ON SCARED DATASET.

Method	Full Image			Masked Region			SSIM(%) ↑	FID↓	TCS↓
	PSNR↑	LPIPS↓	RMSE↓	PSNR↑	LPIPS↓	RMSE↓			
Inpaint_result	31.84	0.100	6.68	27.01	0.017	12.05	90.24	29.92	0.003
Deform3DGS	25.34	0.342	13.83	19.52	0.037	27.19	72.61	74.16	0.027
EndoGaussian	25.96	0.398	12.89	23.56	0.032	17.61	68.39	81.95	0.029
SurgicalGS	24.92	0.434	14.51	21.63	0.040	21.57	65.53	108.89	0.032
Diff2DGS	<u>27.77</u>	<u>0.314</u>	<u>10.53</u>	30.53	<u>0.022</u>	8.21	<u>76.14</u>	<u>61.02</u>	<u>0.027</u>

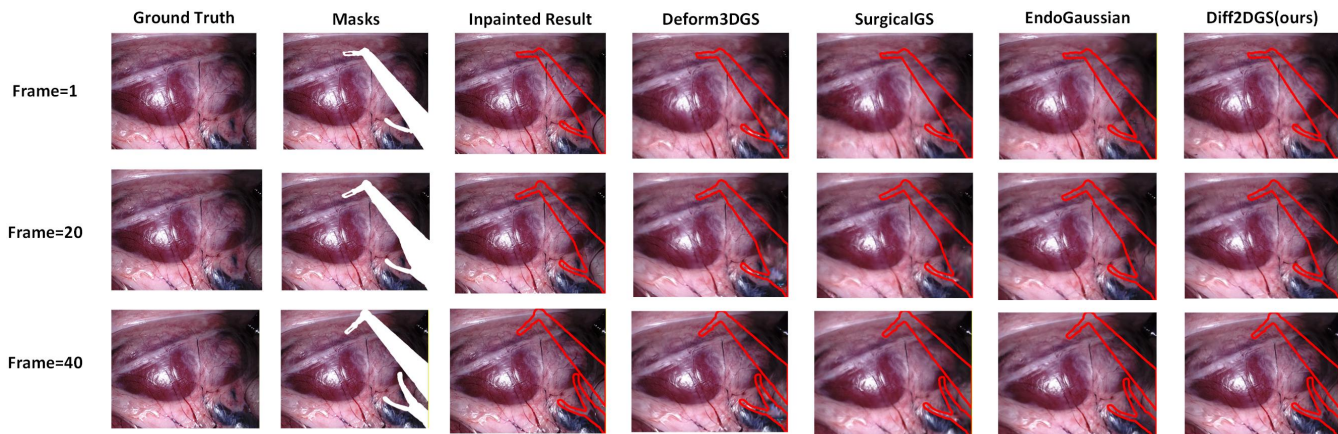


Fig. 5. Visual comparison on SCARED dataset

TABLE IV
ABLATION EXPERIMENT ON STEREOVIS DATASET

Models	PSNR ↑	SSIM(%) ↑
Diffusion+deform3dgs	34.32	90.13
w/o deformation	32.12	86.87
w/o inpainting	31.95	86.11
Diff2dgs(Ours)	34.40	90.72

TABLE V
ERROR ANALYSIS OF RAFT ON SCARED DATASET.

Method	EPE (px) ↓	3 px (%) ↓	MAE (mm) ↓
DLNR [5]	1.45	4.12	1.32
STTR [4]	6.03	9.52	11.31
RAFT [38]	1.16	4.59	1.01



Fig. 6. Ablation experiment on EndoNeRF dataset.

RAFT to estimate depth for inpainted regions. To validate the reliability of RAFT as a reference, we conduct a quantitative error analysis on the SCARED dataset [32], which provides high-quality ground truth depth from structured light scanning.

We compare RAFT against two other state-of-the-art stereo matching methods: DLNR [5] and STTR [4]. The evaluation is performed on the SCARED keyframes, and the results are summarized in Table V. As shown, RAFT achieves the best performance in End-Point-Error (EPE) and Mean Absolute Error (MAE), with an MAE of approximately 1.01 mm, demonstrating its high accuracy for surgical scene reconstruction. This superior performance justifies our choice of RAFT as a reliable depth reference for evaluating the quality of recovered regions.

IV. CONCLUSION

In this paper, we propose Diff2DGS, a reliable surgical scene reconstruction framework designed to address occlusion challenges. By combining 2D Gaussian Splatting with a

Learnable Deformation Model (LDM), we achieve efficient and accurate reconstruction of deformable surgical scenes. Our approach leverages a temporally consistent diffusion model to inpaint regions occluded by instruments, providing high-fidelity supervision for Gaussian initialization. Furthermore, an adaptive depth loss weighting strategy is introduced to dynamically balance appearance and geometric accuracy during training. Evaluated on the EndoNeRF, StereoMIS, and SCARED datasets, Diff2DGS demonstrates superior performance and real-time rendering speeds. While the current framework primarily addresses tissue deformation under relatively static camera views, future work will incorporate camera motion modeling to enhance reconstruction robustness in scenarios with significant camera movement. Overall, Diff2DGS provides a robust solution for high-fidelity intraoperative scene recovery.

REFERENCES

- [1] F. Liebmann, M von Atzigen, D Stütz, J Wolf, L Zingg, D Suter, N A. Cavalcanti, L Leoty, H Esfandiari, J G. Snedeker *et al.*, "Automatic registration with continuous pose updates for marker-less surgical navigation in spine surgery," *Medical Image Analysis*, vol. 91, p. 103027, 2024.
- [2] E Pelanis, A Teatini, B Eigl, A Regensburger, A Alzaga, R P. Kumar, T Rudolph, D L. Aghayan, C Riediger, N Kvarnström *et al.*,

- “Evaluation of a novel navigation platform for laparoscopic liver surgery with organ deformation compensation using injected fiducials,” *Medical image analysis*, vol. 69, p. 101946, 2021.
- [3] F.-Y. Wang, Z Huang, A Bergman, D Shen, P Gao, M Lingelbach, K Sun, W Bian, G Song, Y Liu *et al.*, “Phased consistency models,” *Advances in neural information processing systems*, vol. 37, pp. 83 951–84 009, 2024.
 - [4] Z Li, X Liu, N Drenkow, A Ding, F X. Creighton, R H. Taylor, and M Unberath, “Revisiting stereo depth estimation from a sequence-to-sequence perspective with transformers,” in *Proceedings of the IEEE/CVF international conference on computer vision*, 2021, pp. 6197–6206.
 - [5] H Zhao, H Zhou, Y Zhang, J Chen, Y Yang, and Y Zhao, “High-frequency stereo matching network,” in *Proceedings of the IEEE/CVF conference on computer vision and pattern recognition*, 2023, pp. 1327–1336.
 - [6] R Zha, X Cheng, H Li, M Harandi, and Z Ge, “Endosurf: Neural surface reconstruction of deformable tissues with stereo endoscope videos,” in *International conference on medical image computing and computer-assisted intervention*. Springer, 2023, pp. 13–23.
 - [7] X Liu, M Stiber, J Huang, M Ishii, G D. Hager, R H. Taylor, and M Unberath, “Reconstructing sinus anatomy from endoscopic video—towards a radiation-free approach for quantitative longitudinal assessment,” in *Medical Image Computing and Computer Assisted Intervention—MICCAI 2020: 23rd International Conference, Lima, Peru, October 4–8, 2020, Proceedings, Part III 23*. Springer, 2020, pp. 3–13.
 - [8] R Tang, L.-F. Ma, Z.-X. Rong, M.-D. Li, J.-P. Zeng, X.-D. Wang, H.-E. Liao, and J.-H. Dong, “Augmented reality technology for preoperative planning and intraoperative navigation during hepatobiliary surgery: A review of current methods,” *Hepatobiliary & Pancreatic Diseases International*, vol. 17, no. 2, pp. 101–112, 2018.
 - [9] C Yang, K Wang, Y Wang, X Yang, and W Shen, “Neural lerplane representations for fast 4d reconstruction of deformable tissues,” in *International Conference on Medical Image Computing and Computer-Assisted Intervention*. Springer, 2023, pp. 46–56.
 - [10] B Mildenhall, P P. Srinivasan, M Tancik, J T. Barron, R Ramamoorthi, and R Ng, “Nerf: Representing scenes as neural radiance fields for view synthesis,” *Communications of the ACM*, vol. 65, no. 1, pp. 99–106, 2021.
 - [11] Y Wang, Y Long, S H. Fan, and Q Dou, “Neural rendering for stereo 3d reconstruction of deformable tissues in robotic surgery,” in *International conference on medical image computing and computer-assisted intervention*. Springer, 2022, pp. 431–441.
 - [12] Y Wang, B Gong, Y Long, S H. Fan, and Q Dou, “Efficient endonef reconstruction and its application for data-driven surgical simulation,” *International Journal of Computer Assisted Radiology and Surgery*, vol. 19, no. 5, pp. 821–829, 2024.
 - [13] Y Huang, B Cui, L Bai, Z Guo, M Xu, and H Ren, “Endo-4dgs: Distilling depth ranking for endoscopic monocular scene reconstruction with 4d gaussian splatting,” *arXiv preprint arXiv:2401.16416*, 2024.
 - [14] G Wu, T Yi, J Fang, L Xie, X Zhang, W Wei, W Liu, Q Tian, and X Wang, “4d gaussian splatting for real-time dynamic scene rendering,” in *Proceedings of the IEEE/CVF Conference on Computer Vision and Pattern Recognition*, 2024, pp. 20 310–20 320.
 - [15] B Kerbl, G Kopanas, T Leimkühler, and G Drettakis, “3d gaussian splatting for real-time radiance field rendering,” *ACM Trans. Graph.*, vol. 42, no. 4, pp. 139–1, 2023.
 - [16] Z Yang, X Gao, W Zhou, S Jiao, Y Zhang, and X Jin, “Deformable 3d gaussians for high-fidelity monocular dynamic scene reconstruction,” in *Proceedings of the IEEE/CVF Conference on Computer Vision and Pattern Recognition*, 2024, pp. 20 331–20 341.
 - [17] Z Li, Z Chen, Z Li, and Y Xu, “Spacetime gaussian feature splatting for real-time dynamic view synthesis,” in *Proceedings of the IEEE/CVF Conference on Computer Vision and Pattern Recognition*, 2024, pp. 8508–8520.
 - [18] A Cao and J Johnson, “Hexplane: A fast representation for dynamic scenes,” in *Proceedings of the IEEE/CVF Conference on Computer Vision and Pattern Recognition*, 2023, pp. 130–141.
 - [19] A Kendall, M Grimes, and R Cipolla, “Posenet: A convolutional network for real-time 6-dof camera relocalization,” in *Proceedings of the IEEE international conference on computer vision*, 2015, pp. 2938–2946.
 - [20] S Yang, Q Li, D Shen, B Gong, Q Dou, and Y Jin, “Deform3dgs: Flexible deformation for fast surgical scene reconstruction with gaussian splatting,” in *International Conference on Medical Image Computing and Computer-Assisted Intervention*. Springer, 2024, pp. 132–142.
 - [21] Y Liu, C Li, C Yang, and Y Yuan, “Endogaussian: Gaussian splatting for deformable surgical scene reconstruction,” *arXiv e-prints*, pp. arXiv–2401, 2024.
 - [22] L Yang, B Kang, Z Huang, X Xu, J Feng, and H Zhao, “Depth anything: Unleashing the power of large-scale unlabeled data,” in *Proceedings of the IEEE/CVF Conference on Computer Vision and Pattern Recognition*, 2024, pp. 10 371–10 381.
 - [23] J Wu, X Li, C Si, S Zhou, J Yang, J Zhang, Y Li, K Chen, Y Tong, Z Liu *et al.*, “Towards language-driven video inpainting via multimodal large language models,” in *Proceedings of the IEEE/CVF Conference on Computer Vision and Pattern Recognition*, 2024, pp. 12 501–12 511.
 - [24] Z Zhang, B Wu, X Wang, Y Luo, L Zhang, Y Zhao, P Vajda, D Metaxas, and L Yu, “Avid: Any-length video inpainting with diffusion model,” in *Proceedings of the IEEE/CVF Conference on Computer Vision and Pattern Recognition*, 2024, pp. 7162–7172.
 - [25] B Gu, H Luo, S Guo, and P Dong, “Advanced video inpainting using optical flow-guided efficient diffusion,” *arXiv preprint arXiv:2412.00857*, 2024.
 - [26] M Lee, S Cho, C Shin, J Lee, S Yang, and S Lee, “Video diffusion models are strong video inpainter,” *arXiv preprint arXiv:2408.11402*, 2024.
 - [27] B Huang, Z Yu, A Chen, A Geiger, and S Gao, “2d gaussian splatting for geometrically accurate radiance fields,” in *ACM SIGGRAPH 2024 conference papers*, 2024, pp. 1–11.
 - [28] M Hayoz, C Hahne, M Gallardo, D Candinas, T Kurmann, M Allan, and R Sznitman, “Learning how to robustly estimate camera pose in endoscopic videos,” *International journal of computer assisted radiology and surgery*, vol. 18, no. 7, pp. 1185–1192, 2023.
 - [29] S Imambi, K B. Prakash, and G Kanagachidambaresan, “Pytorch,” *Programming with TensorFlow: solution for edge computing applications*, pp. 87–104, 2021.
 - [30] J Song, C Meng, and S Ermon, “Denoising diffusion implicit models,” *arXiv preprint arXiv:2010.02502*, 2020.
 - [31] J Chen, X Zhang, M I. Hoque, F Vasconcelos, D Stoyanov, D S. Elson, and B Huang, “SurgicalGS: Dynamic 3D Gaussian Splatting for Accurate Robotic-Assisted Surgical Scene Reconstruction,” in *proceedings of Medical Image Computing and Computer Assisted Intervention – MICCAI 2025*, vol. LNCS 15970. Springer Nature Switzerland, September 2025.
 - [32] M Allan, J Mcleod, C Wang, J C. Rosenthal, Z Hu, N Gard, P Eisert, K X. Fu, T Zeffiro, W Xia *et al.*, “Stereo correspondence and reconstruction of endoscopic data challenge,” *arXiv preprint arXiv:2101.01133*, 2021.
 - [33] J Song, J Wang, L Zhao, S Huang, and G Dissanayake, “Dynamic reconstruction of deformable soft-tissue with stereo scope in minimal invasive surgery,” *IEEE Robotics and Automation Letters*, vol. 3, no. 1, pp. 155–162, 2017.
 - [34] T Song, J Cao, K Wang, B Liu, and X Zhang, “Causal-story: Local causal attention utilizing parameter-efficient tuning for visual story synthesis,” in *ICASSP 2024-2024 IEEE International Conference on Acoustics, Speech and Signal Processing (ICASSP)*. IEEE, 2024, pp. 3350–3354.
 - [35] H Zhou and J Jagadeesan, “Real-time dense reconstruction of tissue surface from stereo optical video,” *IEEE transactions on medical imaging*, vol. 39, no. 2, pp. 400–412, 2019.
 - [36] J Choe, S Im, F Rameau, M Kang, and I S. Kweon, “Volumefusion: Deep depth fusion for 3d scene reconstruction,” in *Proceedings of the IEEE/CVF international conference on computer vision*, 2021, pp. 16 086–16 095.
 - [37] X Li, H Xue, P Ren, and L Bo, “Diffuseraser: A diffusion model for video inpainting,” *arXiv preprint arXiv:2501.10018*, 2025.
 - [38] Z Teed and J Deng, “Raft: Recurrent all-pairs field transforms for optical flow,” in *European conference on computer vision*. Springer, 2020, pp. 402–419.